

Scaling of stagnant-lid convection with Arrhenius rheology and the effects of mantle melting

Jun Korenaga

Department of Geology and Geophysics, Yale University, New Haven, CT, USA. E-mail: jun.korenaga@yale.edu

Accepted 2009 May 26. Received 2009 May 18; in original form 2008 December 12

SUMMARY

On the basis of numerical modelling and scaling analysis, a few modifications are proposed for the scaling of stagnant-lid convection, in order to make it more applicable to the thermal evolution of terrestrial planets. The effect of using Arrhenius rheology, as opposed to more popular linear-exponential rheology, is first investigated, and the stability analysis of top thermal boundary layer is shown to be able to capture systematic differences caused by the different kinds of temperature-dependent viscosity. The local stability analysis is then extended to handle the effects of mantle melting such as dehydration stiffening and compositional buoyancy. A new heat-flow scaling law incorporating these effects suggests that mantle melting may reduce the conventional prediction of surface heat flux by up to a factor of ~ 5 –10, and its potential impact on our understanding of planetary evolution is briefly discussed.

Key words: Dynamics of lithosphere and mantle; Heat generation and transport; Rheology; mantle; Planetary interiors.

1 INTRODUCTION

Thermal convection with temperature-dependent viscosity is known to exhibit the stagnant-lid regime (i.e. the top boundary is essentially immobile) when the temperature dependency is sufficiently high (e.g. Morris & Canright 1984; Ogawa *et al.* 1991; Solomatov 1995). Because the viscosity of silicate rocks is strongly temperature-dependent with the activation energy of a few hundred kJ mol^{-1} (Karato & Wu 1993), and because terrestrial planets other than Earth do not show clear evidence for the operation of plate tectonics (Schubert *et al.* 2001), the scaling of stagnant-lid convection has commonly been used when modelling the thermal evolution of these planets (e.g. Solomatov & Moresi 1996; Grasset & Parmentier 1998; Reese *et al.* 1999; Hauck & Phillips 2002).

The cooling history of a planetary mantle controls its chemical evolution via melting, and the chemical evolution could in turn affect the cooling history; melting extracts heat-producing elements from the mantle (Spohn 1991) and results in compositionally buoyant lithosphere (Parmentier & Hess 1992). Mantle melting also dehydrates and stiffens the shallow part of the mantle (Hirth & Kohlstedt 1996). With purely temperature-dependent viscosity, higher mantle temperature implies a thinner lid and thus higher surface heat flux. Hotter mantle, however, starts to melt deeper and creates a thicker dehydrated (and presumably stiff) boundary layer (Korenaga 2003), which may result in a substantial reduction in surface heat flux. Melting-induced viscosity stratification thus has a potential to reshape the scaling of stagnant-lid convection. If there were no water in the mantle, melting would of course produce no viscous stratification (and convection would be sluggish throughout the mantle because of high viscosity expected for a completely dry mantle). Though the amount of water within the planetary mantle

is generally poorly constrained (e.g. Johnson *et al.* 1991; Mysen *et al.* 1998), likely scenarios for planetary accretion suggest that the planetary mantle could have initially been moderately wet as Earth's oceanic upper mantle (i.e. a few hundred ppm H/Si) (e.g. Wänke & Dreibus 1994; Lunine *et al.* 2003), so it would be desirable to take into account the effect of dehydration when modelling planetary evolution.

Recently, van Thienen (2007) has studied the scaling of thermal convection with dehydration stiffening as well as compositional buoyancy, but his study is limited mostly to weakly temperature-dependent viscosity with the maximum viscosity contrast of 100 (equivalent to the activation energy of $\sim 12 \text{ kJ mol}^{-1}$). It is difficult to extract scaling laws relevant to planetary evolution from such modelling results. In this study, therefore, I will focus on convection with strongly temperature-dependent viscosity. By combining simple numerical modelling with scaling analysis, it will be shown that the heat-flow scaling of stagnant-lid convection may be accurately derived from the stability of the top boundary layer alone, even when realistic complications, such as Arrhenius rheology and dehydration stiffening, are incorporated. This simple result is important to build a versatile method of predicting surface heat loss from a chemically differentiating planet.

This paper is organized as follows. First, the effect of using Arrhenius rheology, instead of more popular linear-exponential rheology, on the scaling of stagnant-lid convection will be discussed in some detail. These two types of rheology result in slightly different scaling laws, and a scaling analysis based on boundary layer stability will be introduced to explain the observed difference. Then, the effect of dehydration stiffening will be investigated by introducing depth-dependent viscosity to stagnant-lid convection. The earlier scaling analysis will be shown to be capable of handling this effect as well,

and based on this success, a more general boundary-layer approach will be developed to take into account the effect of compositional buoyancy. Finally, heat-flow scaling for terrestrial planets will be suggested, along with its implications and limitations.

2 LINEAR-EXPONENTIAL VERSUS ARRHENIUS RHEOLOGY

The viscosity of a planetary mantle may be expressed as follows:

$$\eta = \frac{b}{\tau^{n-1}} \exp\left(\frac{E + pV}{RT}\right), \quad (1)$$

where b is a pre-exponential factor, τ is the second invariant of stress, n is the stress exponent, E is the activation energy, p is pressure, V is the activation volume, R is the universal gas constant and T is absolute temperature. The stress exponent is one for diffusion creep, and is typically $\sim 3-5$ for dislocation creep. Different deformation mechanisms have different activation energies and volumes as well. Whereas multiple deformation mechanisms can take place in parallel (known as composite rheology), eq. (1) assumes only one mechanism, so it should be regarded as the simplest form of mantle rheology. As will be shown, our understanding has not been established even in this case; more realistic cases of composite rheology are left for future studies.

Eq. (1) may be non-dimensionalized as

$$\eta^* = (\tau^*)^{1-n} \exp\left(\frac{E^*}{T^* + T_{\text{off}}^*} - \frac{E^*}{1 + T_{\text{off}}^*}\right), \quad (2)$$

where asterisks denote non-dimensionalized quantities. Here temperature is normalized as

$$T^* = \frac{T - T_s}{\Delta T}, \quad (3)$$

where T_s is the surface temperature and ΔT is the temperature contrast across the mantle. The parameter T_{off}^* is the surface temperature normalized by the temperature contrast, $T_s/\Delta T$ and $E^* = E/(R\Delta T)$. For simplicity, the activation volume is neglected hereinafter.

In the numerical studies of mantle convection, the Arrhenius rheology has often been approximated by the following linear-exponential viscosity:

$$\eta^* = (\tau^*)^{1-n} \exp[\theta(1 - T^*)], \quad (4)$$

where θ is the Frank–Kamenetskii parameter defined as

$$\theta = \frac{E\Delta T}{R(T_s + \Delta T)^2} = \frac{E^*}{(1 + T_{\text{off}}^*)^2}. \quad (5)$$

At $T^* = 1$, the linear-exponential viscosity defined this way has the same temperature dependency as the original Arrhenius form, but they diverge quickly as $T^* \rightarrow 0$ (Fig. 1). There are a few reasons why the linear-exponential approximation is popular. First, it is numerically more tractable because of smaller viscosity contrast and more amenable to theoretical analyses because of its simpler functionality. Second, it has only one parameter to vary (i.e. θ) whereas the Arrhenius rheology has three (E , T_s and ΔT) (Fig. 1). Even with the use of a realistic activation energy, therefore, one can still achieve an unrealistically small viscosity contrast by controlling other two parameters (e.g. Tackley 2000). Such ambiguity is absent for linear-exponential viscosity. Finally, it is a particularly good approximation for stagnant-lid convection because only a bottom fraction of the top boundary layer with $T^* \sim 1$ (called the rheological sublayer) participates in convection. The scaling

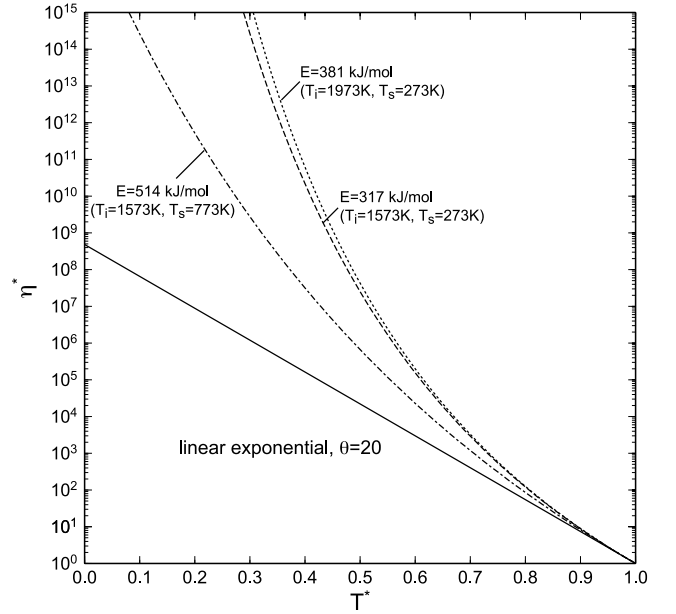


Figure 1. Comparison of linear-exponential rheology (eq. 4) and Arrhenius rheology (eq. 2). All examples shown have the same Frank–Kamenetskii parameter θ of 20. The relation between θ and activation energy E is not unique because the Frank–Kamenetskii parameter depends also on surface temperature T_s and temperature contrast ΔT (eq. 5).

laws of stagnant-lid convection have commonly been derived with the Frank–Kamenetskii parameter (e.g. Davaille & Jaupart 1993; Grasset & Parmentier 1998; Solomatov & Moresi 2000). Nevertheless, it is the Arrhenius rheology that describes the temperature dependency of mantle viscosity because thermally activated processes take the Arrhenius form, and it is desirable to know how good the linear-exponential approximation would be. Reese *et al.* (1999) conducted a direct comparison of these two viscosity laws and concluded that the efficiency of heat transport is about 20 per cent lower for the Arrhenius rheology, but their analysis is based on numerical results with only one set of model parameters. A more systematic attempt is reported in this section. Because only a small temperature contrast is involved in stagnant-lid convection, the difference between the two types of rheology is expected to be small. My intention to scrutinize this issue is to derive the systematics of such subtle difference, which can serve as a testing ground for developing an accurate scaling theory. The strategy of numerical modelling follows closely that of Solomatov & Moresi (2000), but to set up notations for subsequent discussion, theoretical formulation will be given in a self-contained manner.

2.1 Theoretical formulation

The non-dimensionalized governing equations for thermal convection of an incompressible fluid with internal heat generation consist of the conservation of mass,

$$\nabla \cdot \mathbf{u}^* = 0, \quad (6)$$

the conservation of momentum,

$$-\nabla P^* + \nabla \cdot [\eta^*(\nabla \mathbf{u}^* + \nabla \mathbf{u}^{*T})] + RaT^* \mathbf{e}_z = 0, \quad (7)$$

and the conservation of energy,

$$\frac{\partial T^*}{\partial t^*} + \mathbf{u}^* \cdot \nabla T^* = \nabla^2 T^* + H^*. \quad (8)$$

The unit vector pointing upward is denoted by \mathbf{e}_z . The spatial coordinates are normalized by the depth of a fluid layer, D , and time is normalized by the diffusion timescale, D^2/κ , where κ is thermal diffusivity. Velocity \mathbf{u}^* is thus normalized by κ/D . Temperature is normalized by the temperature scale ΔT , and viscosity is by a reference viscosity η_0 . The definitions of ΔT and η_0 are different for the exponential and Arrhenius cases, and they will be explained in more detail. Dynamic pressure P^* and heat generation H^* are normalized by $\eta_0\kappa/D$ and $\rho_0 D^2/(k\Delta T)$, respectively, where ρ_0 is reference density and k is thermal conductivity. The Rayleigh number Ra is defined as

$$Ra = \frac{\alpha\rho_0 g\Delta T D^3}{\kappa\eta_0}, \quad (9)$$

where α is thermal expansivity and g is gravitational acceleration.

Following Solomatov & Moresi (2000), purely internal heating is adopted; that is, the bottom boundary is insulated. There will be no thermal boundary layer at the bottom, simplifying the scaling analysis of numerical results. At the same time, however, the internal temperature (the temperature of convecting mantle beneath the stagnant lid) is not known *a priori*. For convection with internal heating, therefore, it is common to extract the temperature scale from heat generation as

$$\Delta T_H = \frac{\rho_0 H D^2}{k}, \quad (10)$$

and use viscosity at the surface temperature as the reference viscosity. With this temperature scale, the non-dimensional heat generation H^* in eq. (8) becomes unity. The following (dimensional) form of exponential viscosity is used:

$$\eta = \frac{b}{\tau^{n-1}} \exp(-\gamma T), \quad (11)$$

which may be non-dimensionalized as

$$\eta^* = (\tau^*)^{1-n} \exp(-\theta_H T^*), \quad (12)$$

where θ_H is $\gamma\Delta T_H$ and the reference viscosity is given by

$$\eta_0 = b^{1/n} \left(\frac{D^2}{\kappa}\right)^{(n-1)/n}. \quad (13)$$

Using eqs (10) and (13), the Rayleigh number may be expressed as

$$Ra_{H,0} = \frac{\alpha\rho^2 g H D^{(3n+2)/n}}{k b^{1/n} \kappa^{1/n}}, \quad (14)$$

which is called the surface Rayleigh number because the reference viscosity is defined at the surface temperature. The internal temperature, T_i , is usually calculated based on the horizontally averaged temperature profile, $\langle T \rangle$ (Fig. 2). If we use the difference between the internal temperature and the surface temperature to redefine the temperature scale (i.e. $\Delta T = T_i - T_s$), then, the viscosity may be expressed as

$$\eta^* = (\tau^*)^{1-n} \exp(-\theta T^*), \quad (15)$$

where

$$\theta = \frac{\Delta T}{\Delta T_H} \theta_H. \quad (16)$$

Eq. (15) is the same as eq. (4) except for the factor e^θ . Using this new temperature scale and viscosity at the internal temperature, the internal Rayleigh number is defined as

$$Ra_i = \frac{\alpha\rho g\Delta T D^{(n+2)/n}}{b^{1/n}\kappa^{1/n} \exp(-\gamma T_i/n)}. \quad (17)$$

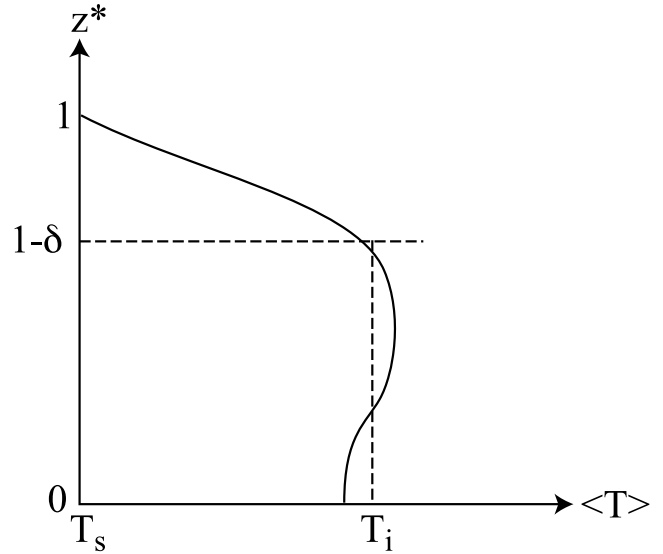


Figure 2. Schematic illustration of the relation among horizontally averaged temperature $\langle T \rangle$, internal temperature T_i and the thickness of thermal boundary layer δ , for internally heated convection. Temperature variations with depth are exaggerated.

Because of purely internal heating, the surface heat flux q is equal to total heat generation in the fluid divided by surface area,

$$q = \rho_0 D H, \quad (18)$$

and the corresponding Nusselt number is given by

$$Nu = \frac{q}{k\Delta T/D} = \frac{\Delta T_H}{\Delta T}. \quad (19)$$

The internal temperature is thus fundamental to calculating the internal Rayleigh number and the Nusselt number. Because the horizontally average temperature usually exhibits small fluctuations with depth (Fig. 2), however, how to define T_i is not very unique. It is not described by Solomatov & Moresi (2000). One may define the base of the stagnant lid based on the velocity profile and take the average of temperature below the lid. Here, I choose to rely solely on temperature and define T_i in a self-consistent manner as

$$T_i - T_s = \frac{1}{1-\delta} \int_0^{1-\delta} \langle T \rangle dz^*, \quad (20)$$

where $\delta = Nu^{-1} = (T_i - T_s)/\Delta T_H$. The non-dimensionalized thickness of the top thermal boundary layer is the reciprocal of the Nusselt number, and the internal temperature is defined as the average of temperature below the boundary layer. For a given temperature profile $\langle T \rangle$, the above equation is solved numerically for T_i .

For the Arrhenius rheology, eq. (1) is used. Its non-dimensional form (eq. 2) assumes that the reference viscosity is defined at the internal temperature and also that temperature is normalized by $\Delta T (= T_i - T_s)$. So Ra in eq. (7) corresponds to the internal Rayleigh number defined as

$$Ra_i = \frac{\alpha\rho g\Delta T D^{(n+2)/n}}{b^{1/n}\kappa^{1/n} \exp[E/(nRT_i)]}. \quad (21)$$

Heat generation H^* in eq. (8) must be chosen properly so that the normalized internal temperature T_i^* is unity, and it may be obtained as follows. Each model run with the exponential viscosity is associated with the Frank–Kamenetskii parameter θ (eq. 16), Ra_i (eq. 17)

and Nu (eq. 19). The activation energy E for a corresponding Arrhenius case is calculated from θ based on eq. (5) (Here, I arbitrarily use $T_s = 273$ K and $\Delta T = 1500$ K.), and if the linear-exponential approximation were exact, running such Arrhenius case with $Ra = Ra_i$ and $H^* = Nu$ should result in $T_i^* = 1$. In reality, T_i^* slightly deviates from unity, so the following *a posteriori* rescaling is necessary:

$$\Delta T = \Delta T_{\text{orig}} T_i^*, \quad (22)$$

$$Nu = Nu_{\text{orig}} / T_i^*, \quad (23)$$

$$Ra_i = Ra_{i,\text{orig}} T_i^* \exp\left(\frac{E^*}{1 + T_{\text{off}}^*} - \frac{E^*}{T_i^* + T_{\text{off}}^*}\right)^{1/n}, \quad (24)$$

$$T^* = T_{\text{orig}}^* / T_i^*. \quad (25)$$

2.2 Numerical results

The finite element code of Korenaga & Jordan (2003) was used to solve the coupled Stokes flow and thermal advection-diffusion eqs (6)–(8). To avoid wall effects, the aspect ratio of the convection model is set to 4, and the model domain is discretized with 128×32 uniform 2-D quadrilateral elements. The non-dimensional surface

temperature is fixed to zero, and the bottom boundary is insulated. The top and bottom boundaries are free-slip, and a reflecting boundary condition is applied to the side boundaries. A total of 32 runs were conducted with the linear-exponential viscosity, with the same combinations of n , θ_H and $Ra_{H,0}$ used by Solomatov & Moresi (2000) (Table 1). Numerical results reported here thus serve as a benchmark test of the code of Korenaga & Jordan (2003) in terms of finite-amplitude convection with non-linear viscosity. Each run was started with an initial temperature field of the following form:

$$T^*(x^*, z^*) = c + a \cos(\pi x^*) \sin(\pi z^*), \quad (26)$$

where the constants c and a were set to 0.2 and 0.05, respectively, in most cases, and was integrated until $t^* = 3$. The influence of the initial condition disappeared for $t^* > \sim 0.5$ –1, and model statistics was taken using the interval of $t^* = 1 - 3$.

Compared to Solomatov & Moresi (2000), Nu is systematically higher by ~ 0.5 –2 per cent (Table 1), suggesting that the self-consistent definition of T_i (eq. 20) results in slightly lower values than what Solomatov & Moresi (2000) obtained. The root-mean-square (rms) velocity for the entire model domain, v_{rms} , is not affected by such difference in the definition of T_i and indeed exhibits no systematic difference. On average, the velocity measurement is different from that of Solomatov & Moresi (2000) by ~ 2 per cent (Table 1), which is comparable to 2–3 per cent error estimated by

Table 1. Numerical results for cases with purely temperature-dependent viscosity.

n	Linear exponential				Arrhenius ^b					
	θ_H	$Ra_{H,0}$	Nu^a	$v_{\text{rms}}^{*,a}$	E^c	ΔT	θ	Ra_i	Nu	v_{rms}^*
1	40	10	3.09 (3.03)	71 (76)	230	1531	13.0	2.41×10^6	2.94	81
1	50	1	3.11 (3.06)	94 (103)	280	1522	15.9	5.13×10^6	2.96	111
1	50	3	3.28 (3.25)	119 (119)	270	1546	15.2	7.18×10^6	3.20	144
1	50	10	3.52 (3.50)	137 (137)	250	1549	14.0	7.52×10^6	3.39	160
1	50	30	3.78 (3.75)	150 (147)	230	1528	13.0	6.38×10^6	3.44	153
1	50	100	4.12 (4.09)	171 (167)	210	1561	11.7	8.36×10^6	3.84	199
1	60	0.1	3.13 (3.10)	135 (138)	340	1531	19.2	1.24×10^7	3.04	166
1	60	0.3	3.29 (3.27)	157 (151)	320	1537	18.1	1.36×10^7	3.22	187
1	60	1	3.50 (3.48)	173 (172)	300	1544	16.9	1.49×10^7	3.40	212
1	60	3	3.70 (3.69)	193 (187)	280	1546	15.7	1.57×10^7	3.59	235
1	60	10	3.98 (3.97)	213 (201)	260	1561	14.5	1.72×10^7	3.84	265
1	60	30	4.28 (4.24)	226 (223)	250	1564	13.9	1.89×10^7	4.03	292
2	50	10	2.78 (2.75)	47 (47)	317	1537	17.9	4.14×10^4	2.63	50
2	50	30	3.10 (3.06)	60 (61)	285	1556	15.9	4.81×10^4	2.95	71
2	50	100	3.56 (3.50)	80 (80)	249	1574	13.8	5.31×10^4	3.34	97
2	60	3	2.80 (2.78)	61 (62)	376	1525	21.3	6.35×10^4	2.66	62
2	60	10	3.10 (3.07)	80 (80)	341	1543	19.2	7.73×10^4	2.98	94
2	60	30	3.45 (3.41)	101 (99)	307	1558	17.2	8.42×10^4	3.28	121
2	70	1	2.86 (2.83)	81 (81)	431	1528	24.4	1.06×10^5	2.78	94
2	70	3	3.09 (3.07)	103 (102)	397	1536	22.4	1.17×10^5	3.00	120
2	70	10	3.41 (3.38)	129 (127)	361	1545	20.3	1.29×10^5	3.28	155
2	70	30	3.77 (3.73)	155 (152)	327	1556	18.3	1.39×10^5	3.60	190
3	60	30	2.95 (2.88)	56 (56)	360	1552	20.2	1.31×10^4	2.80	62
3	70	3	2.52 (2.50)	43 (43)	490	1524	27.8	1.65×10^4	2.46	46
3	70	10	2.85 (2.80)	63 (65)	430	1530	24.3	1.80×10^4	2.74	72
3	70	30	3.23 (3.15)	85 (86)	390	1545	21.9	2.05×10^4	3.11	106
3	70	100	3.78 (3.68)	113 (112)	330	1564	18.4	2.03×10^4	3.55	136
3	80	1	2.51 (2.49)	49 (51)	560	1525	31.8	2.19×10^4	2.46	55
3	80	3	2.75 (2.71)	70 (72)	510	1522	29.0	2.34×10^4	2.66	76
3	80	10	3.09 (3.04)	95 (98)	460	1530	26.0	2.54×10^4	2.94	106
3	80	30	3.49 (3.42)	123 (122)	400	1540	22.5	2.63×10^4	3.31	140
3	80	100	4.06 (3.95)	154 (154)	350	1548	19.6	2.80×10^4	3.78	186

^aNumbers in parentheses are from Solomatov & Moresi (2000) for comparison.

^b T_s is 273 K for all cases.

^cUnit is kJ mol^{-1} .

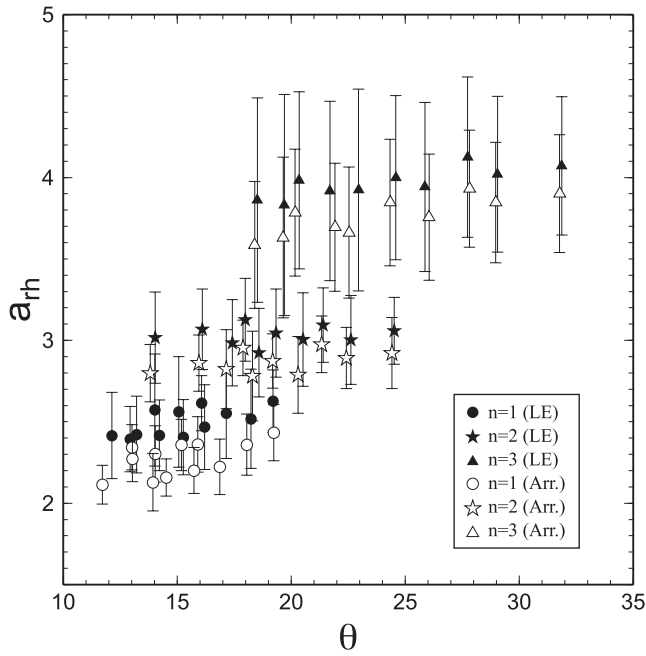


Figure 3. Measured logarithmic viscosity contrast within the convecting region beneath the stagnant lid, a_{th} , for linear-exponential (solid symbols) and Arrhenius (open) cases reported in Table 1. Error bars denote one standard deviation and are mostly due to fluctuations in temperature at the lid base.

them. The base of the stagnant lid is defined using a tangent at the inflection point z_i^* of the velocity profile as

$$z_L^* = z_i^* - \frac{v_{\text{rms}}^*(z_i^*)}{(v_{\text{rms}}^*)'(z_i^*)}, \quad (27)$$

where the prime denotes spatial differentiation. Then, the lid thickness d_L^* is given by $1 - z_L^*$. The logarithmic viscosity contrast within the convecting region beneath the lid is calculated as

$$a_{\text{th}} = \log \frac{\eta[\langle T \rangle(z_L^*)]}{\eta(T_i)} = \theta_H [T_i^* - \langle T^* \rangle(z_L^*)], \quad (28)$$

where temperature is normalized by ΔT_H . The viscosity contrast is nearly constant for the same stress exponent, and a_{th} is ~ 2.5 ($n = 1$), ~ 3.0 ($n = 2$) and ~ 4.0 ($n = 3$) (Fig. 3). These values are smaller than reported by Solomatov & Moresi (2000), probably because of different definitions for T_i . Temperature at the lid base is more time-dependent than the internal temperature, resulting in relatively large uncertainty for a_{th} (Fig. 3). The lid thickness d_L^* , which is based on the velocity profile, is similar to the thickness of the thermal boundary layer δ , and the former may be better suited to measure kinematic observables such as the internal viscosity contrast.

For each exponential-viscosity case, a corresponding Arrhenius-viscosity model was run as described in Section 2.1, and results are summarized in Table 1. The logarithmic viscosity contrast a_{th} is slightly smaller than the exponential case: ~ 2.3 ($n = 1$), ~ 2.9 ($n = 2$) and ~ 3.7 ($n = 3$) (Fig. 3), which is expected from the superexponential behaviour of the Arrhenius rheology (Fig. 1).

2.3 Scaling analysis

Heat-flow scaling for internally heated stagnant-lid convection may be expressed as (e.g. Reese *et al.* 1999; Solomatov & Moresi 2000)

$$Nu[1 - 2Nu^{-1}(1 - a_{\text{th}}\theta^{-1})]^{1-\beta(n+2)/(2n)} = a\theta^{-1-\beta} Ra_i^\beta, \quad (29)$$

where $\beta = n/(n + 2)$. In the limit of $Nu \gg 1$, it approaches the following asymptotic formula:

$$Nu \approx a\theta^{-1-\beta} Ra_i^\beta. \quad (30)$$

Solomatov & Moresi (2000) fit eq. (29) to their numerical results and obtained $a \approx 0.31 + 0.22n$ by assuming $a_{\text{th}} = 1.2(n + 1)$. As my definition of T_i (eq. 20) results in slightly different values of Nu , Ra_i and a_{th} , I repeated their regression analysis and obtained that $a \approx 0.30 + 0.25n$. The rms error of the fit is ~ 1.2 per cent (Fig. 4a).

Similarly, velocity scaling has often been assumed as

$$v_{\text{rms}}^* = a_v [1 - 2Nu^{-1}(1 - a_{\text{th}}\theta^{-1})]^b \left(\frac{Ra_i}{\theta} \right)^{\beta_v}, \quad (31)$$

where

$$b = \frac{\beta_v(n + 2)}{2n} \quad (32)$$

and

$$\beta_v = \frac{n(2n + 1)}{(n + 1)(n + 2)}. \quad (33)$$

The asymptotic form is as follows:

$$v_{\text{rms}}^* \approx a_v \left(\frac{Ra_i}{\theta} \right)^{\beta_v}. \quad (34)$$

The expression for the exponent b is, however, inconsistent with the rms operation assumed for v_{rms}^* . The correct expression is the following:

$$b = \frac{\beta_v(n + 2)}{2n} - \frac{1}{4}. \quad (35)$$

With this correction, I fit eq. (31) to numerical data and obtained $a_v \approx 0.05 + 0.29/n$. The rms error is ~ 4.4 per cent (Fig. 4b). The difference from the previous result, $0.04 + 0.34/n$, is trivial, but the correct form of b turns out to be important when comparing the exponential and Arrhenius runs.

The purpose of the Arrhenius runs is to derive minimum possible corrections to eqs (29) and (31). To this end, these equations were solved for the effective Frank–Kamenetskii parameter θ_{eff} using Nu and Ra_i from the Arrhenius runs. That is, the parameters a_{th} , a and a_v take the aforementioned values determined by the exponential-viscosity data. The correction factor $\theta_{\text{eff}}/\theta$ is plotted in Fig. 4(c) (based on eq. 29) and Fig. 4(d) (based on eq. 31). It was found that eq. (35) is essential to obtain similar correction factors for both heat-flow scaling and velocity scaling. If eq. (32) is used instead, the correction factor for velocity scaling would be very different from that for heat-flow scaling. The factor is generally in the range of ~ 1.15 – 1.35 , encompassing the value of 1.2 suggested by Reese *et al.* (1999).

The correction factor may be justified as follows. From eq. (28), a temperature contrast in the convecting region beneath the lid can be related to a_{th} as

$$\Delta T_e^* = \frac{a_{\text{th}}^L}{\theta} \quad (36)$$

for the linear-exponential viscosity as signified by the superscript L . Here temperature is normalized by ΔT . One may derive a similar expression for the Arrhenius viscosity as

$$\Delta T_e^* = \frac{a_{\text{th}}^A}{\theta + a_{\text{th}}^A/(1 + T_{\text{off}}^*)}, \quad (37)$$

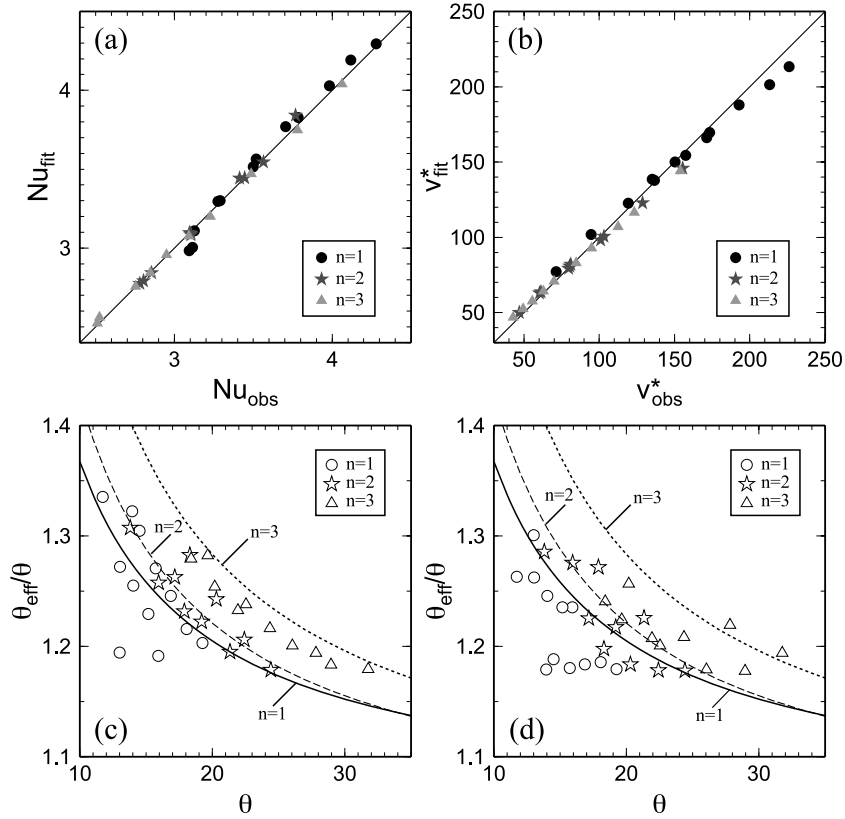


Figure 4. (a) The results of fitting the heat-flow scaling of eq. (29) to the Nusselt number observed for the linear-exponential runs reported in Table 1. Fitting was done separately for a subgroup of runs with the same n , and the fitted values of a are 0.57 ($n = 1$), 0.79 ($n = 2$) and 1.05 ($n = 3$). (b) Same as (a) but for the velocity scaling of eq. (31). The fitted values of a_v are 0.35 ($n = 1$), 0.18 ($n = 2$) and 0.16 ($n = 3$). (c) The correction factor $\theta_{\text{eff}}/\theta$ based on fitting the Arrhenius results to the heat-flow scaling of eq. (29). Curves are theoretical prediction based on eq. (41) with $T_s = 273$ K and $\Delta T = 1500$ K. (d) Same as (c) but with the velocity scaling of eq. (31).

where the superscript A denotes Arrhenius. Equating the above with $a_{\text{rh}}^L/\theta_{\text{eff}}$ leads to

$$\frac{\theta_{\text{eff}}}{\theta} = \frac{a_{\text{rh}}^L(n)}{a_{\text{rh}}^A(n)} \left[1 + \frac{a_{\text{rh}}^A(n)}{\theta(1 + T_{\text{off}}^*)} \right] \equiv c_1. \quad (38)$$

Alternatively, the effective Frank–Kamenetskii parameter may be defined by a viscosity gradient at the lid base as

$$\theta_{\text{eff}} = \frac{E^*}{(1 - \Delta T_e^* + T_{\text{off}}^*)^2}, \quad (39)$$

which may be rearranged to

$$\frac{\theta_{\text{eff}}}{\theta} = \left[1 + \frac{a_{\text{rh}}^A(n)}{\theta(1 + T_{\text{off}}^*)} \right]^2 \equiv c_2. \quad (40)$$

Either expression can explain measured correction factors reasonably well for $n = 1$, but c_1 tends to be too low for higher n whereas c_2 too high. Thus, their geometric mean is adopted as an optimal choice

$$\frac{\theta_{\text{eff}}}{\theta} = (c_1 c_2)^{1/2}. \quad (41)$$

Even with the above, only a modest fit to measured values is achieved (Figs 4c and d), but this may be understood from large uncertainties associated with a_{rh} (Fig. 3).

The heat-flow scaling law in the asymptotic limit (eq. 30) can be derived from the stability analysis of the top thermal boundary layer (e.g. Solomatov 1995). Consider a boundary layer of thickness δ , in which normalized temperature increases linearly from 0 to 1

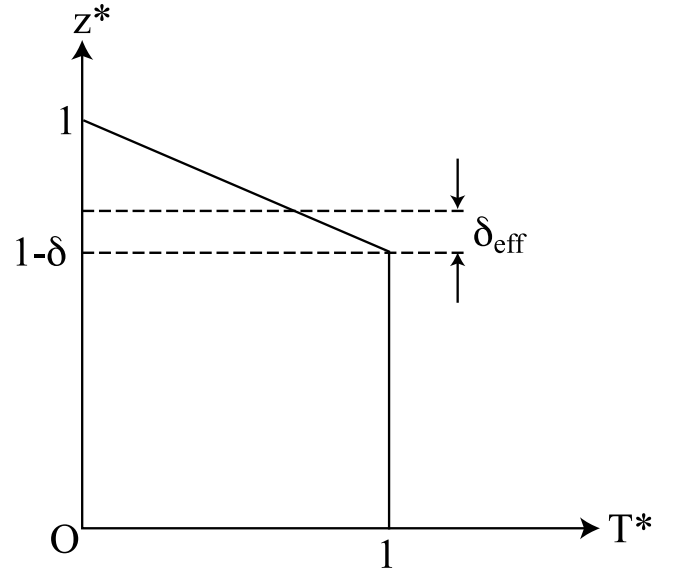


Figure 5. Schematic illustration of a model setup for the local stability analysis of the thermal boundary layer.

(Fig. 5). The local Rayleigh number for the boundary layer may be defined as

$$Ra_l(\delta) = Ra_i \max_{\delta_{\text{eff}}} \left[\frac{\delta_{\text{eff}}^{(n+2)/n} \Delta T_{\text{eff}}^*}{(n_{\text{eff}}^*)^{1/n}} \right], \quad (42)$$

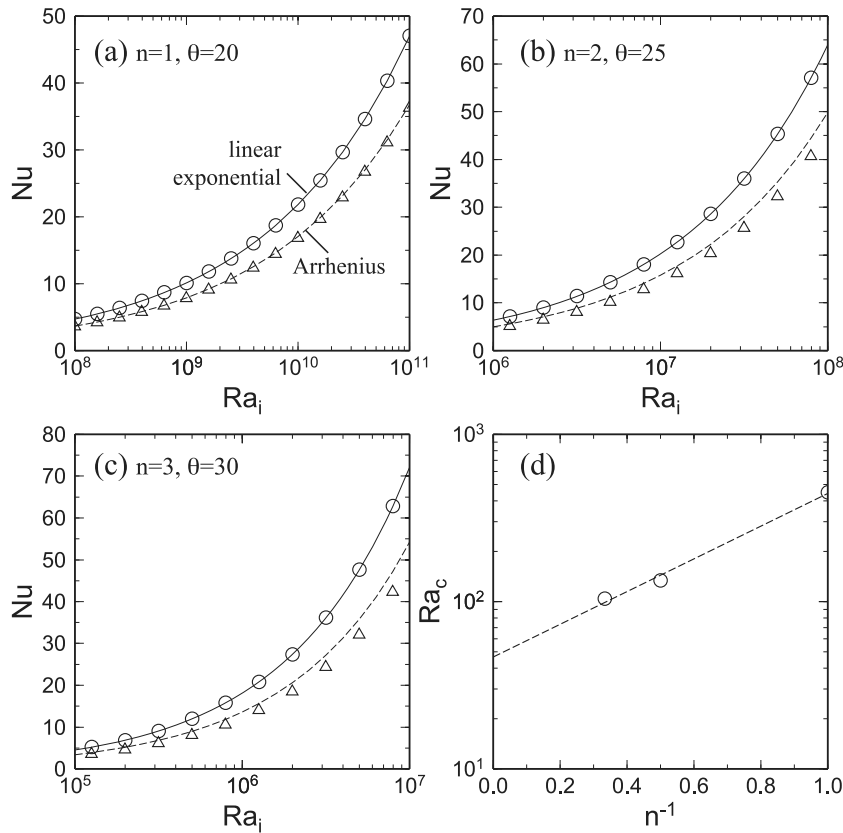


Figure 6. (a)–(c) Comparison of Nu prediction based on local stability analysis (symbols) with the asymptotic scaling law (curves). For linear-exponential rheology, the scaling law of eq. (30) is used, and it is modified with the correction factor of eq. (41) for Arrhenius rheology. Three different combinations of n and θ are considered. (d) The critical Rayleigh numbers estimated from the asymptotic heat-flow scaling are shown as symbols for $n = 1$ – 3 , and the fitted formula of eq. (44) is shown as dashed line.

where Ra_i is the internal Rayleigh number for the entire domain, δ_{eff} is the thickness of a sublayer that varies from 0 to δ , ΔT_{eff}^* is an effective temperature contrast within the sublayer ($= \delta_{\text{eff}}/\delta$) and η_{eff}^* is effective viscosity for the sublayer. A logarithmic average is used to calculate η_{eff}^* . The thickness of the thermal boundary layer in stagnant-lid convection may be considered as the maximum thickness that a boundary layer can achieve before becoming dynamically unstable, that is,

$$Ra_i(\delta) = Ra_{\text{crit}}(n), \quad (43)$$

where $Ra_{\text{crit}}(n)$ is the critical Rayleigh number as a function of the stress exponent n . Thus, $Nu (= \delta^{-1})$ can be derived by combining eqs (42) and (43) if $Ra_{\text{crit}}(n)$ is known.

Eq. (30) with $a \approx 0.30 + 0.25n$ implies that the critical Rayleigh number is ~ 450 ($n = 1$), ~ 134 ($n = 2$) and ~ 104 ($n = 3$), and a general expression is estimated as (Fig. 6d)

$$Ra_{\text{crit}}(n) \approx \exp(3.84 + 2.25/n). \quad (44)$$

With this critical Rayleigh number, the boundary-layer stability approach reproduces exactly the asymptotic heat-flow scaling in the case of linear-exponential viscosity (Figs 6a–c). This stability analysis can easily be extended to the Arrhenius viscosity; only η_{eff}^* in eq. (42) requires modification. Using the same critical Rayleigh number, the local stability approach also reproduces well the heat-flow scaling for the Arrhenius viscosity, though it tends to underpredict when $n > 1$ (Figs 6a–c). The simplicity of the stability analysis and its capability of capturing the subtle difference between the exponential and Arrhenius cases suggest that this approach may

be further extended to handle more involved situations, as will be shown in the next sections.

3 EFFECTS OF MANTLE MELTING

As mentioned in Section 1, mantle melting likely introduces viscosity and compositional stratifications in the shallow mantle. The dry solidus for an Earth-like mantle may be expressed as (Takahashi & Kushiro 1983)

$$P_0 = (T_p - 1150)/100, \quad (45)$$

where P_0 is the initial pressure of melting in GPa and T_p is the potential temperature (hypothetical temperature of mantle adiabatically brought to the surface without melting) in °C. An upwelling mantle with T_p of 1350 °C, for example, starts to melt at the pressure of 2 GPa. A trace amount of water if present causes mantle melting at a slightly higher pressure, but the above dry solidus is sufficient to provide a conservative estimate on the effects of mantle melting. For Earth, the pressure of 2 GPa corresponds to the depth of 60 km. This length scale is comparable with that of the thermal boundary layer. The pressure would correspond to greater depths for smaller planets such as Mars and Mercury. Thus, the effects of mantle melting on planetary evolution are expected to be more significant for smaller terrestrial planets.

3.1 Dehydration stiffening

An increase in viscosity caused by the loss of hydrogen upon melting is on the order of 10^2 – 10^3 for dislocation creep (e.g. Hirth & Kohlstedt 1996; Mei & Kohlstedt 2000b; Korenaga & Karato 2008) and ~ 10 for diffusion creep (e.g. Mei & Kohlstedt 2000a; Korenaga & Karato 2008). Faul & Jackson (2007) recently suggested that nominally dry deformation experiments may be influenced by a trace amount of melt and that melt-free diffusion creep is two orders of magnitude slower. If this is the case, diffusion creep would also exhibit a factor of $\sim 10^3$ increase in viscosity due to dehydration.

Because hydrogen is highly incompatible with the solid phase (e.g. Koga *et al.* 2003), the residual solid component of an upwelling mantle would be almost completely dehydrated as soon as it starts to melt (Hirth & Kohlstedt 1996). Dehydration stiffening thus results in step-function-like viscosity stratification; that is, viscosity increases by a few orders of magnitude within a narrow depth interval. The presence of partial melt can somewhat compensate this viscosity increase, but its porosity is expected to be low because melt is more buoyant than the coexisting solid at shallow upper mantle conditions and starts to form an interconnected network at a very low porosity (< 1 per cent) (Kohlstedt 1992). The influence of partial melt on dehydration stiffening is thus expected to be minor (e.g. Braun *et al.* 2000). The melt phase will eventually drain away because of its positive buoyancy unless it is continuously supplied from below; such situation would be possible only when the mantle is somehow heating up (instead of cooling down) during planetary evolution.

Whereas several authors have investigated stagnant-lid convection with depth-dependent viscosity caused by non-zero activation volume (eq. 1) (e.g. Doin *et al.* 1997; Dumoulin *et al.* 1999), step-function-like depth dependency has so far received little attention. A sudden viscosity increase by mantle melting cannot be approximated well by the use of activation volume, which results in a gradual viscosity increase over the entire model depth. Here the linear-exponential viscosity of eq. (15) is modified as

$$\eta^* = (\tau^*)^{1-n} Z(z^*) \exp(-\theta T^*), \quad (46)$$

where

$$Z(z^*) = \begin{cases} 1 & \text{for } z^* \leq z_D^* \\ \Delta\eta & \text{for } z^* > z_D^* \end{cases} \quad (47)$$

and z_D^* marks the base of dehydrated mantle. This depth dependency is time-independent. Alternatively, one could mark the dehydrated part of the mantle and trace its advection through time. Though this would be dynamically more self-consistent, tracing chemistry is time-consuming and makes the problem setup less clean. Even with the time-independent viscosity stratification, modelling would be self-consistent if convection is restricted to $z^* < z_D^*$, and as shown later, self consistency can easily be achieved at the stage of scaling analysis.

Numerical modelling similar to that reported in Section 2.2 was conducted with the viscosity of eq. (46). The initial and boundary conditions as well as the aspect ratio are the same as before, but the model domain is discretized by 192×48 uniform elements to handle runs with higher Rayleigh numbers. Each run was again integrated to $t^* = 3$, and results for $t^* > 1$ were averaged to yield model statistics. One Newtonian ($n = 1$) and one non-Newtonian ($n = 3$) models are considered, and for both models, z_D^* is set to 0.75. Three different viscosity contrasts (1, 3 and 10) are used, and the runs with $\Delta\eta = 1$ are used as a reference. For purely internal heating, the internal temperature (and thus θ) cannot be known *a priori*, so it is difficult to collect model results with some fixed value

Table 2. Numerical results for cases with temperature- and depth-dependent viscosity ($n = 1$ and $\theta_H = 50$).

$Ra_{H,0}$	$\Delta\eta^a$	θ	Ra_i	d_L^*	Nu	v_{rms}^*
1	1	16.05	2.99×10^6	0.32	3.12	95
3	1	15.11	3.31×10^6	0.30	3.31	109
10	1	14.12	3.84×10^6	0.27	3.54	130
30	1	13.18	4.19×10^6	0.25	3.79	148
100	1	12.11	4.41×10^6	0.22	4.13	167
300	1	11.11	4.45×10^6	0.20	4.50	182
1000	1	10.02	4.50×10^6	0.17	4.99	202
3000	1	9.03	4.51×10^6	0.15	5.54	221
10000	1	7.93	4.40×10^6	0.12	6.31	242
30000	1	6.93	4.23×10^6	0.10	7.22	262
1	3	16.16	3.38×10^6	0.33	3.09	101
3	3	15.29	3.99×10^6	0.31	3.27	117
10	3	14.36	4.97×10^6	0.28	3.48	140
30	3	13.60	6.61×10^6	0.27	3.68	170
100	3	12.85	9.75×10^6	0.25	3.89	214
300	3	12.10	1.31×10^7	0.24	4.13	256
1000	3	10.98	1.28×10^7	0.22	4.56	278
3000	3	10.03	1.37×10^7	0.20	4.98	308
10000	3	8.95	1.39×10^7	0.19	5.58	331
30000	3	7.96	1.37×10^7	0.13	6.28	355
1	10	16.14	3.31×10^6	0.33	3.10	98
3	10	15.31	4.11×10^6	0.31	3.26	118
10	10	14.44	5.38×10^6	0.29	3.46	143
30	10	13.74	7.65×10^6	0.27	3.64	177
100	10	13.10	1.28×10^7	0.26	3.82	235
300	10	12.59	2.21×10^7	0.25	3.97	308
1000	10	12.05	4.12×10^7	0.25	4.15	409
3000	10	11.12	4.52×10^7	0.24	4.50	445
10000	10	10.06	4.69×10^7	0.23	4.97	489
30000	10	8.99	4.34×10^7	0.22	5.56	499

^aViscosity contrast for $z^* > 0.75$ ($\Delta\eta$ of 1 denotes no depth-dependency).

of θ ; to do so, modelling must be run iteratively. Instead, a series of model runs were conducted with a fixed θ_H and a range of $Ra_{H,0}$ (Tables 2 and 3). Though θ varies for different values of $Ra_{H,0}$, it is straightforward to extract the effect of depth-dependent viscosity from any model run because a corresponding reference case without depth-dependent viscosity can be predicted by the scaling law of eq. (29) with reasonable accuracy.

Some snapshots from the Newtonian model are shown in Fig. 7. As $Ra_{H,0}$ increases, the thermal boundary layer becomes thinner, and Nu increases. An increase in $Ra_{H,0}$ does not always lead to an increase in Ra_i (e.g. Fig. 8a), because higher $Ra_{H,0}$ tends to be compensated by lower internal temperature thus higher viscosity. Thus, the observed increase in Nu is mostly due to a decrease in θ . The effect of depth-dependent viscosity may not be easily recognized in Fig. 7, but for example, the cases of $Ra_{H,0} = 100$ and 1000 with $\Delta\eta = 10$ indicate that the gradual thinning of the boundary layer is prevented by the increased viscosity for $z^* > 0.75$. It is also seen that the viscosity contrast of 10 is too small to maintain the integrity of the dehydrated lid for higher $Ra_{H,0}$.

Model results can be interpreted more clearly by comparing with reference states. For each model run, the following two references may be defined. Both references assume purely temperature-dependent, exponential viscosity and share the same θ as the model run under consideration. One has the same Ra_i (i.e. the same interior viscosity) as well, but the other has it reduced by a factor of $\Delta\eta$. That is, the first reference (denoted by the superscript +) corresponds to a case without dehydration stiffening, and the second (denoted by the superscript –) to a case in which the mantle

Table 3. Numerical results for cases with temperature- and depth-dependent viscosity ($n = 3$ and $\theta_H = 80$).

$Ra_{H,0}$	$\Delta\eta^a$	θ	Ra_i	d_L^*	Nu	v_{rms}^*
3	1	28.98	1.71×10^4	0.39	2.76	71
6	1	27.15	1.74×10^4	0.35	2.95	86
10	1	25.78	1.74×10^4	0.33	3.10	97
20	1	23.91	1.73×10^4	0.30	3.35	113
30	1	22.85	1.74×10^4	0.28	3.50	123
60	1	20.97	1.71×10^4	0.25	3.81	140
100	1	19.58	1.67×10^4	0.22	4.09	154
200	1	17.68	1.60×10^4	0.20	4.52	173
300	1	16.58	1.56×10^4	0.18	4.82	185
600	1	14.68	1.47×10^4	0.15	5.45	206
1000	1	13.28	1.39×10^4	0.13	6.03	223
3	3	28.97	1.70×10^4	0.39	2.76	70
6	3	27.16	1.74×10^4	0.35	2.95	85
10	3	25.82	1.76×10^4	0.33	3.10	97
20	3	24.07	1.84×10^4	0.30	3.32	116
30	3	23.12	1.93×10^4	0.28	3.46	129
60	3	21.63	2.19×10^4	0.26	3.70	157
100	3	20.65	2.52×10^4	0.25	3.87	185
200	3	19.30	3.01×10^4	0.23	4.14	226
300	3	18.14	2.87×10^4	0.22	4.41	240
600	3	15.95	2.43×10^4	0.19	5.02	254
1000	3	14.45	2.23×10^4	0.16	5.54	265
3	10	28.96	1.69×10^4	0.39	2.76	71
6	10	27.17	1.75×10^4	0.35	2.94	86
10	10	25.86	1.79×10^4	0.33	3.09	98
20	10	24.12	1.87×10^4	0.30	3.32	117
30	10	23.20	1.99×10^4	0.29	3.45	130
60	10	21.82	2.36×10^4	0.27	3.67	163
100	10	21.00	2.88×10^4	0.26	3.81	196
200	10	20.10	4.08×10^4	0.25	3.98	262
300	10	19.62	5.10×10^4	0.24	4.08	310
600	10	17.62	4.70×10^4	0.23	4.54	339
1000	10	15.78	3.79×10^4	0.21	5.07	337

^aViscosity contrast for $z^* > 0.75$ ($\Delta\eta$ of 1 denotes no depth-dependency).

is entirely dry. Surface heat flux and convective velocity should be bounded by these two references, that is, $Nu^- \leq Nu \leq Nu^+$ and $v_i^{*-} \leq v_i^* \leq v_i^{*+}$, where v_i^* denotes rms velocity beneath the lid and may be calculated as $v_{\text{rms}}^*/\sqrt{1 - Nu^{-1}}$. This is approximately the case in Figs 8 and 9; the violation of these bounds observed in Fig. 9(a) is due to the finite accuracy of the heat-flow scaling law. Important observations are (1) that the presence of a dehydrated lid reduces surface heat flux even when the dehydrated lid is thinner than the (purely temperature-dependent) stagnant lid, that is, $Nu < Nu^+$ even when $Nu^+ < 1/z_D^*$; (2) that the dehydrated lid is eventually destabilized when the internal Rayleigh number is so high that even the entirely dry mantle yields a thinner stagnant lid, that is, $Nu \approx Nu^-$ when $Nu^- > 1/z_D^*$; and (3) that the velocity scaling for the first reference may provide a reasonable approximation as long as the dehydrated lid is stable, that is, $v_i^* \approx v_i^{*+}$ when $Nu < 1/z_D^*$.

The first two observations regarding heat-flow scaling can be reproduced well by the boundary-layer stability analysis (Fig. 10); the depth-dependent viscosity of eq. (46) is used when calculating η_{eff}^* in eq. (42). We may symbolically express this boundary-layer-based prediction as

$$Nu = F_{Nu}(n, \theta, Ra_i, \Delta\eta, z_D^*), \quad (48)$$

and when the dehydrated layer becomes dynamically unstable, that is, $Nu > 1/z_D^*$, we can modify the depth-dependent viscosity to be

self-consistent and solve the following equation recursively:

$$Nu = F_{Nu}(n, \theta, Ra_i, \Delta\eta, Nu^{-1}), \quad (49)$$

until Nu converges. The convergence is usually achieved within a few iterations. For the examples shown in Fig. 10, the use of the recursive formula resulted in trivial differences (< 0.1 per cent), suggesting that the time-independent depth dependency does not pose a major problem as far as heat-flow scaling is concerned.

3.2 Compositional buoyancy

Residual mantle after melt extraction is less dense than unmelted mantle, and for an Earth-like mantle, this compositional effect may be expressed as (Korenaga 2006)

$$\left(\frac{d\rho}{dF}\right) \approx -1.2 \text{ kg m}^{-3} / \text{per cent}, \quad (50)$$

where F is the degree of melting. The mean degree of melting may be defined as

$$\bar{F} = 0.5(P_0 - P_f) \left(\frac{dF}{dP}\right)_S, \quad (51)$$

where P_f is the final pressure of melting and $(dF/dP)_S$ is a change in melt fraction with a change in pressure above the solidus during adiabatic decompression. Combined with the solidus of eq. (45), the mean degree of melting can be estimated as a function of potential temperature (Fig. 11). Density stratification introduced by mantle melting is then given by

$$\rho^*(z^*) = \begin{cases} 1 & \text{for } z^* \leq z_D^* \\ \Delta\rho & \text{for } z^* > z_D^*, \end{cases} \quad (52)$$

where

$$\Delta\rho = 1 + \frac{\bar{F}}{\rho_0} \left(\frac{d\rho}{dF}\right). \quad (53)$$

This is a rough approximation because the degree of melting is likely to be stratified within the depleted lid (i.e. shallower mantle is more depleted and less dense), but it would be sufficient to provide an order-of-magnitude estimate.

The significance of the density contrast $\Delta\rho$ (Fig. 11) may be appreciated by calculating an equivalent temperature contrast, ΔT_ρ^* , which is defined through

$$\begin{aligned} \rho^*(z^*, T^*) &= \rho^*(z^*)[1 + \alpha\Delta T(1 - T^*)] \\ &= 1 + \alpha\Delta T(1 - T^* - \Delta T_\rho^*). \end{aligned} \quad (54)$$

The factor $\alpha\Delta T$ is ~ 0.05 , so $\Delta\rho$ of 0.99 corresponds to ΔT_ρ^* of ~ 0.2 . Translating the density contrast of a compositional origin into the equivalent temperature contrast is also meaningful from the perspective of convective instability. The Rayleigh number (eq. 9) is the ratio of the diffusion timescale over the advection timescale,

$$Ra = \frac{D^2/\kappa}{\eta/(\alpha\rho g\Delta T D)}, \quad (55)$$

and the advection timescale is determined by the balance between viscous resistance ($\propto \eta$) and thermal buoyancy ($\propto \alpha\rho g\Delta T$). Thus, the effect of compositional buoyancy on the stability of the thermal boundary layer (and thus heat-flow scaling) may be considered most naturally by calculating ‘effective’ thermal buoyancy. This can be done if ΔT_ρ^* is incorporated when calculating ΔT_{eff}^* in eq. (42).

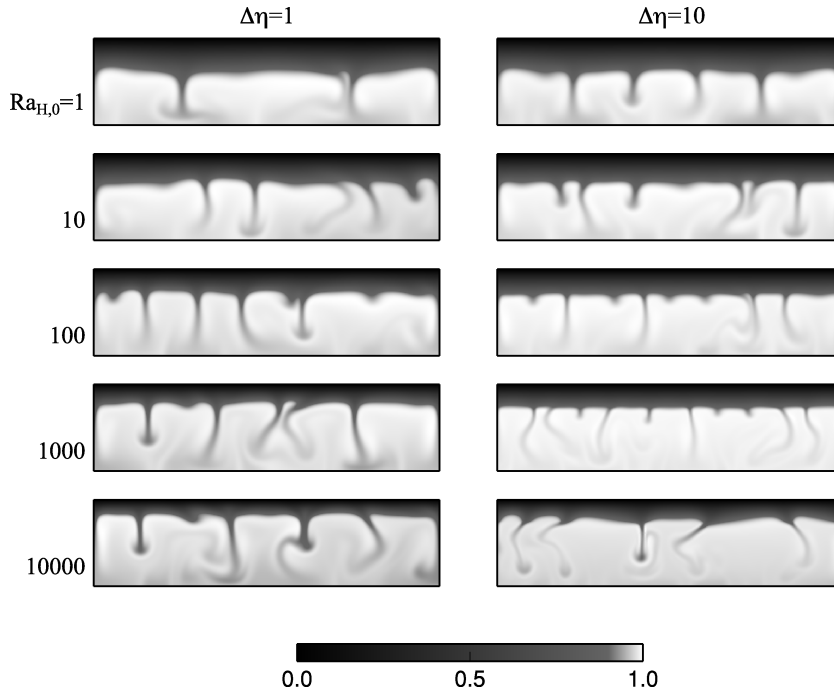


Figure 7. Some snapshots of the temperature field from numerical simulation reported in Table 2 ($n = 1$ and $\theta_H = 50$). Temperature is normalized by $\Delta T = T_i - T_s$. The left-hand panel shows purely temperature-dependent viscosity runs ($\Delta\eta = 1$) for five different values of $Ra_{H,0}$. The right-hand panel shows temperature- and depth-dependent viscosity runs ($\Delta\eta = 10$ with $z_D^* = 0.75$).

4 APPLICATION TO MANTLE CONVECTION IN TERRESTRIAL PLANETS

To illustrate the potential impact of mantle melting on planetary evolution, some dimensionalized examples will be presented in this section. The boundary-layer stability criterion (eq. 43) is used to calculate Nu , and this may be symbolically expressed as

$$Nu = F_{Nu}(n, E, T_s, \Delta T, Ra_i, \Delta\eta, \Delta\rho, z_D^*), \quad (56)$$

which signifies that the Arrhenius rheology of eq. (1) is used. The surface heat flux can then be obtained as $q = Nuk\Delta T/D$ (eq. 19). The following values are assumed for all examples: $k = 4 \text{ W m}^{-1} \text{ K}^{-1}$, $\alpha = 2 \times 10^{-3} \text{ K}^{-1}$, $\kappa = 10^{-6} \text{ m}^2 \text{ s}^{-2}$ and $\rho_0 = 4000 \text{ kg m}^{-3}$. To calculate melting-related parameters such as P_0 and $\Delta\rho$, ρ_0 of 3300 kg m^{-3} is used. The activation energy E is set to 300 kJ mol^{-1} for $n = 1$ and 500 kJ mol^{-1} for $n = 3$, and for both cases, the pre-exponential factor b in eq. (1) is determined so that the surface heat flux is 50 mW m^{-2} at the present-day Earth condition ($D = 2900 \times 10^3 \text{ m}$, $g = 9.8 \text{ m s}^{-2}$, $T_s = 273 \text{ K}$, and $\Delta T = 1350 \text{ K}$) without the effects of mantle melting (i.e. $\Delta\eta = 1$ and $\Delta\rho = 1$). In reality, different deformation mechanisms are expected to result in different surface heat fluxes, and even with the same deformation mechanism, different planets may take different pre-exponential factors because of possible differences in, for example, grain size and mantle composition. As mentioned in Section 2, multiple deformation mechanisms can take place in parallel, which further complicates this issue. The purpose of this (arbitrary) normalization for mantle rheology is to provide a simple reference point and highlight differences caused by mantle melting and the size of a planet. For mantle melting, the dry solidus of eq. (45) is assumed. For an incompressible fluid (as assumed in eqs 6–8), the internal temperature T_i is the potential temperature T_p . The viscosity contrast introduced by dehydration is set to 10^2 ,

and compositional buoyancy is calculated based on Fig. 11. As in Section 3.1, eq. (56) is solved iteratively by setting $z_D^* = Nu^{-1}$ when $Nu > 1/z_D^*$, to have a self-consistent pair of the surface heat flux and the assumed viscosity and density structure.

4.1 Earth

Though Earth does not presently exhibit stagnant-lid convection, the rheology of the (upper) mantle and its melting behavior are best understood for Earth, so it is convenient to use this familiar planet first to derive a hypothetical heat-flow scaling law, against which results for other planets may be compared. Fig. 12 shows the case of Newtonian rheology ($n = 1$). For a likely range of internal temperature for thermal evolution (1200–1800 °C), Ra_i varies from $\sim 10^9$ to $\sim 10^{13}$ (Fig. 12a). The Nusselt number deviates considerably from the conventional scaling of $Ra_i^{1/3}$ (eq. 30) when the effects of mantle melting are considered (Fig. 12b). In particular, the combination of compositional buoyancy and dehydration stiffening reverts completely the sense of the heat-flow scaling for higher Ra_i . As Fig. 12(c) indicates, the thickness of thermal boundary layer δ decreases monotonically with increasing internal temperature in case of conventional, purely temperature-dependent scaling, but such thinning of the boundary layer is countered by thicker depleted lithosphere expected for hotter mantle. When compositional buoyancy and dehydration stiffening are considered separately, the latter has a far greater impact on heat-flow scaling, but when considered jointly, compositional buoyancy seems to play an important role at higher temperatures. Mantle melting thus makes the surface heat flux q relatively insensitive to a change in mantle temperature (Fig. 12d), which resembles closely the scaling of Korenaga (2006) suggested for plate-tectonic convection.

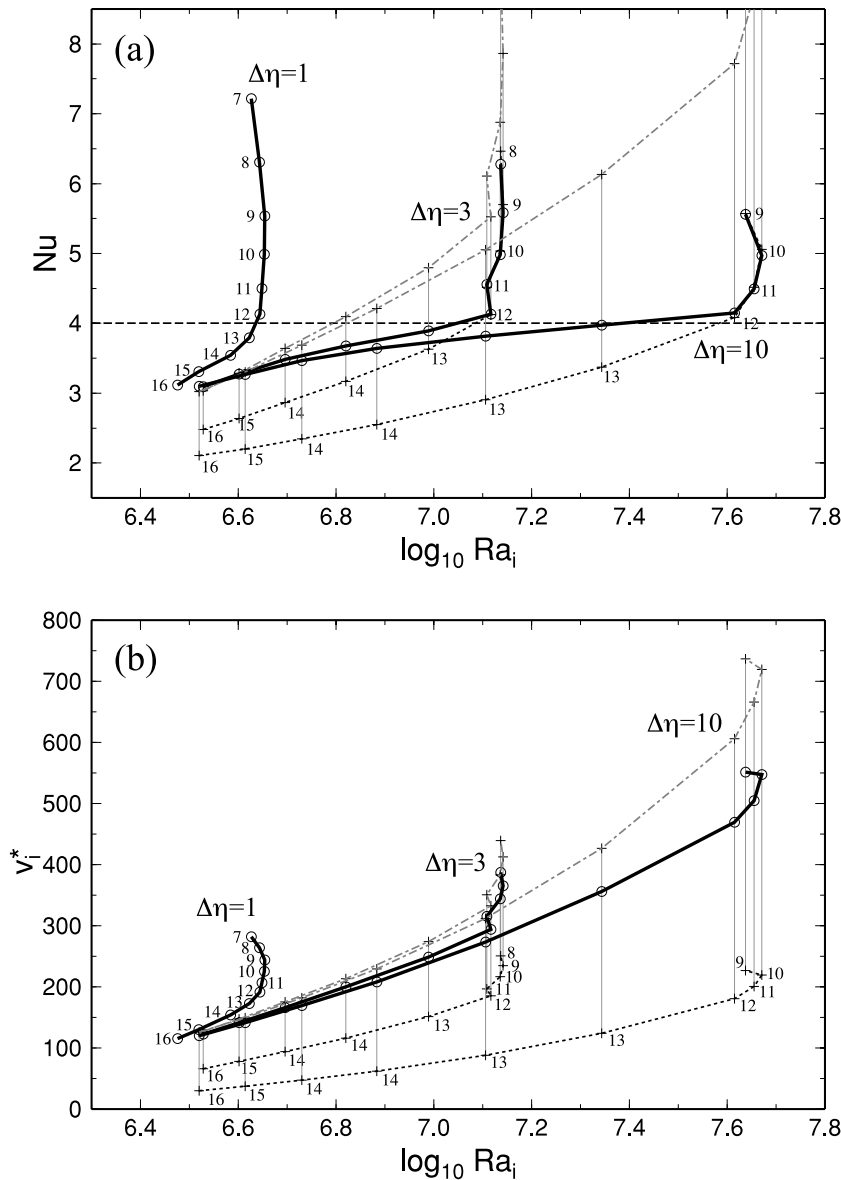


Figure 8. Effects of depth-dependent viscosity on (a) the Nusselt number and (b) interval velocity for the Newtonian rheology case reported in Table 2. Open circles connected by solid lines denote the results of numerical modelling. Dotted lines connect the predicted lower bound (Nu^- and $v_i^{*, -}$) whereas dot-dashed lines connect the upper bound (Nu^+ and $v_i^{*, +}$). The Frank–Kamenetskii parameter θ varies for different model runs and is listed along the lower limit. The upper and lower bounds at the same θ are connected by a vertical line. The horizontal line in (a) corresponds to $Nu = 1/z_D^*$.

4.2 Other terrestrial planets

Three terrestrial planets, Mars, Venus, and a ‘super-Earth’ (e.g. Valencia *et al.* 2007), are considered here to illustrate the effects of planet size (Mars and super-Earth) and surface temperature (Venus). Gravitational acceleration g and mantle depth D for these planets are: 3.7 m s^{-2} and $1800 \times 10^3 \text{ m}$ (Mars), 9.0 m s^{-2} and $2941 \times 10^3 \text{ m}$ (Venus) and 32.3 m s^{-2} and $4060 \times 10^3 \text{ m}$ (super-Earth), respectively. The surface temperature is set to 773 K for Venus and 273 K for others.

The predicted surface heat flux is shown as a function of internal temperature (Fig. 13). Compared with the same viscosity contrast $\Delta\eta$, the effect of dehydration stiffening is more reduced for non-Newtonian rheology, because only the $1/n$ th power of the viscosity contrast contributes to the boundary-layer stability (eq. 42). As ex-

pected, mantle melting starts to affect heat-flow scaling at lower temperatures for Mars than Earth because the low gravity of Mars results in the formation of thicker depleted mantle for a given potential temperature. Depleted mantle may be too thick to be dynamically stable at higher temperatures ($T_i > \sim 1600 \text{ }^\circ\text{C}$), and even the combination of dehydration stiffening and compositional buoyancy cannot maintain the negative temperature sensitivity of surface heat flux (Figs 13a and d), though higher $\Delta\eta$ would help to stabilize the depleted lid. Despite its similar size to Earth, the scaling for Venus is more similar to that for Mars, and this is because its high surface temperature reduces the effective temperature dependency of Arrhenius rheology (e.g. Fig. 1), which would result in a thinner thermal boundary layer in the absence of mantle melting. It is notable that the effects of mantle melting are important even for a ‘super-Earth’ (Figs 13c and f). In general, when compositional

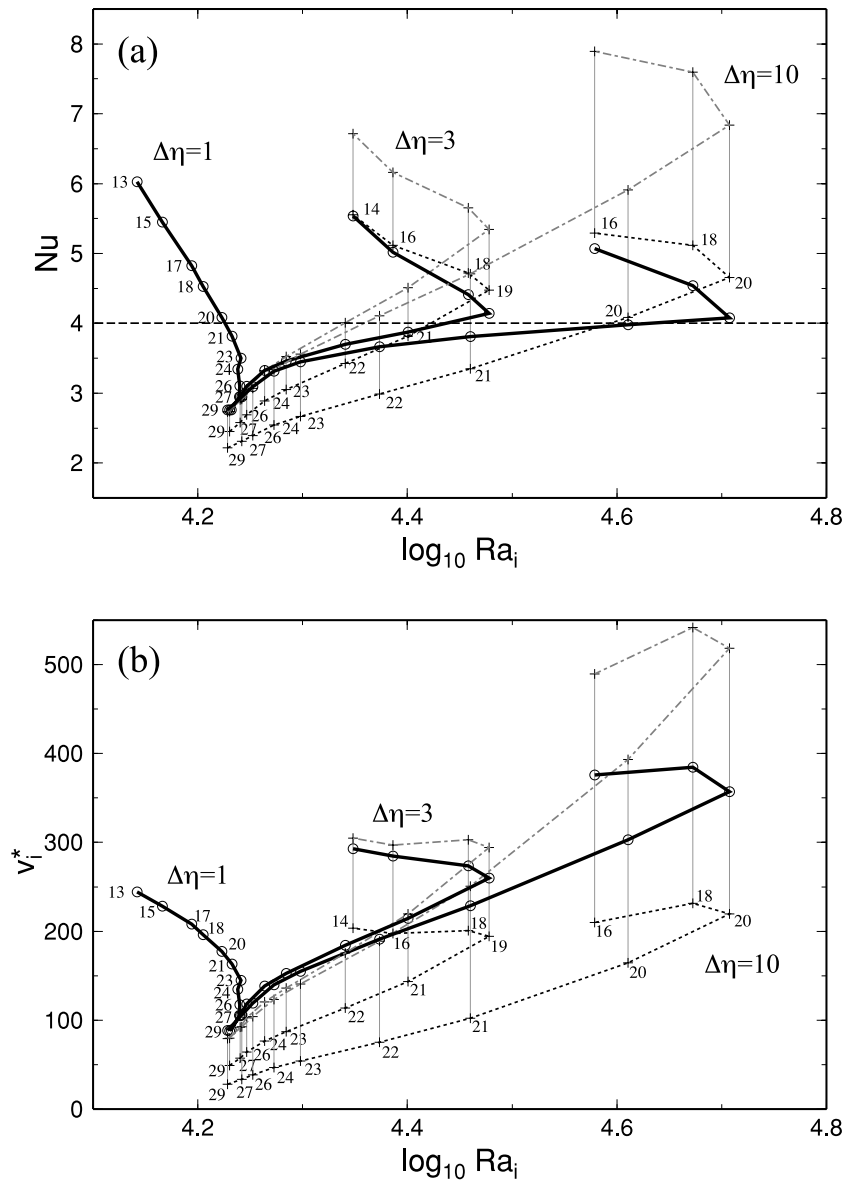


Figure 9. Same as Fig. 8, but for the non-Newtonian rheology case reported in Table 3.

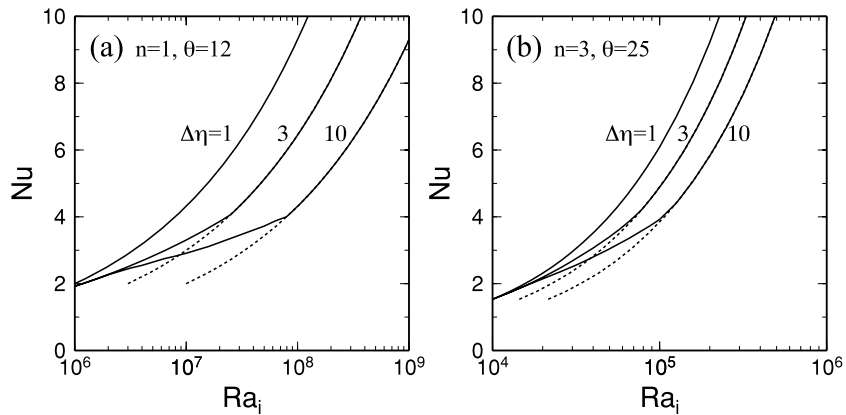


Figure 10. The effect of depth-dependent viscosity on heat-flow scaling as predicted by local stability analysis. (a) Newtonian case ($n = 1$) with $\theta = 12$ and (b) non-Newtonian case ($n = 3$) with $\theta = 25$. Purely temperature-dependent reference ($\Delta\eta = 1$) and two temperature- and depth-dependent cases ($\Delta\eta = 3$ and 10 with $z_D^* = 0.75$) are shown. Dotted curves denote the theoretical lower limit Nu^- . The case of $\Delta\eta = 1$ is equivalent to the upper limit Nu^+ for all cases.

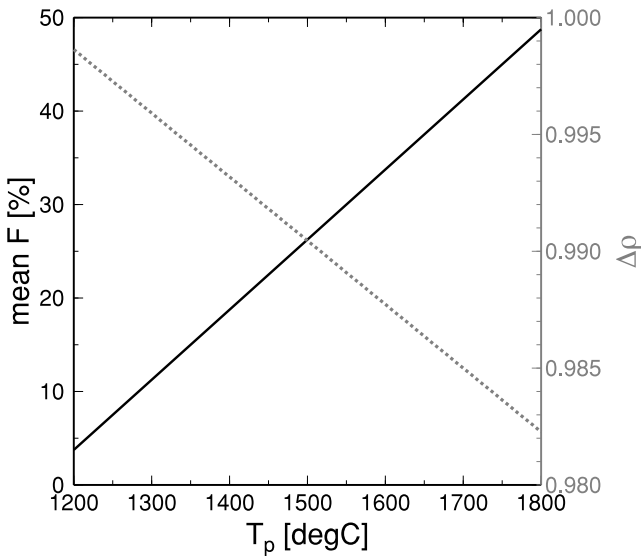


Figure 11. The mean degree of melting (solid) and the normalized density of depleted lid (grey) are shown as a function of mantle potential temperature. Melt productivity $(dF/dP)_S$ is assumed to be 15 per cent/GPa (Korenaga 2006), and for simplicity, the final pressure of melting P_f is set to zero.

buoyancy and dehydration stiffening are considered jointly, mantle melting could reduce the conventional prediction of surface heat flux by up to a factor of ~ 5 –10.

The potential impact of the new scaling laws on the thermal evolution of these planets may be better understood by converting the surface heat flux to the mantle cooling rate as $dT/dt = qS/C_m$, where S is the surface area of a planet and C_m is the heat capacity of the mantle (Fig. 14). With mantle melting, the cooling rate would be substantially reduced when the mantle is very hot, that is, at the early stage of planetary evolution. Mantle cooling directly regulates the thermal history of the core and thus the existence of a planetary magnetic field. The significance of the new scaling laws would be best appreciated when modelling the thermal evolution of terrestrial planets by parameterized convection, and such attempt will be reported elsewhere. It is important to note, however, that the heat-flow scaling of Fig. 13 should not be directly used in parameterized convection; they need to be amended in various ways to cope with realistic complications as discussed in the following sections.

4.3 Rewetting from below by hydrogen diffusion

Though melting is very effective in removing water (or hydrogen) from the mantle, the dehydrated mantle is always underlain by unmelted (wet) mantle, so it is continuously re-hydrated from below by hydrogen diffusion. Because this rehydration could potentially undermine the significance of dehydration stiffening in heat-flow scaling, it is worth considering this diffusion process quantitatively. Chemical diffusion in one dimension may be expressed generally as

$$\frac{\partial C}{\partial t} = \frac{\partial}{\partial z} \left[D(z) \frac{\partial C}{\partial z} \right], \quad (57)$$

where C denotes concentration and $D(z)$ is the diffusion coefficient that may be spatially variable. The diffusion of hydrogen in olivine depends on temperature as

$$D_H(T) = D_{H,0} \exp\left(-\frac{E}{RT}\right), \quad (58)$$

where $D_{H,0} = 6 \times 10^{-5} \text{ m}^2 \text{ s}^{-1}$ and $E = 130 \text{ kJ mol}^{-1}$ (Mackwell & Kohlstedt 1990). These values are for diffusion within a single crystal; diffusion in olivine aggregates could be faster because of grain boundaries, but no experimental constraint is available. The diffusion coefficient varies from $\sim 3 \times 10^{-8} \text{ m}^2 \text{ s}^{-1}$ at $1800 \text{ }^\circ\text{C}$ to $\sim 3 \times 10^{-9} \text{ m}^2 \text{ s}^{-1}$ at $1300 \text{ }^\circ\text{C}$, so diffusion distance could be a few tens of km over billion years. In the colder part of lithosphere, however, diffusion would be much slower; at $1100 \text{ }^\circ\text{C}$, for example, $D_H = \sim 6 \times 10^{-10} \text{ m}^2 \text{ s}^{-1}$, corresponding to the diffusion distance of only $\sim 8 \text{ km}$ for 4 Gyr.

To estimate an ‘effective’ diffusion coefficient for hydrogen diffusion in the top thermal boundary layer, the above diffusion equation was numerically integrated. A linear temperature profile is assumed for the boundary layer (e.g. Fig. 5), which is initially dry (i.e. $C = 0$), and the base of the boundary layer is fixed to a constant hydrogen concentration. This boundary condition is appropriate because the mantle just below the lid is continuously refreshed by convection. The surface temperature is set to 273 K , and a temperature increase across the boundary layer is ΔT . Numerical results are shown in Fig. 15, where distance is normalized by the boundary layer thickness δ and time is by $\delta^2/D_{H,0}$. The results may be captured by the following approximate formula for the non-dimensional diffusion distance:

$$d^* \approx (D_{H,\text{eff}}^* t^*)^{1/2}, \quad (59)$$

where

$$D_{H,\text{eff}}^* = -0.0027 + 2.19 \times 10^{-6} \Delta T, \quad (60)$$

and its dimensional version is given by

$$d \approx (D_{H,\text{eff}}^* D_{H,0} t)^{1/2}. \quad (61)$$

The above approximate formula may be used in parameterized convection modelling to adjust the thickness of the dehydrated lid during time integration. Whereas the lid thickness is continuously reduced by rehydration, however, further mantle melting could recover the original thickness if the mantle is hot enough. The significance of rehydration is thus expected to vary among different scenarios for planetary evolution.

4.4 Other important complications

For heat-flow scaling with mantle melting (Figs 12d and 13), the initial pressure of melting P_0 is used to define the base of the depleted lid at a given internal temperature. This is equivalent to assuming that the depleted lid achieves its maximum possible thickness ‘globally’, and the plausibility of this assumption rests on the vigor of convection beneath the stagnant lid. The globally averaged lid thickness may not reach the upper limit if convection is too slow to efficiently differentiate the mantle. The velocity scaling of eq. (34) with the correction factor $\theta_{\text{eff}}/\theta$ (eq. 41) would be useful to track the growth of the depleted lid in parameterized convection.

Also, contrary to what Figs 12(c) implies, the thickness of the depleted lid does not have to decrease as the internal temperature decreases. If the mantle melts efficiently and the maximum lid thickness is achieved at some high temperature during the very early phase of planetary evolution, the thick lid could suppress further melting because a colder mantle does not melt beneath the lid. Because the thermal history of a terrestrial planet usually starts at an initially high mantle temperature, surface heat flux could be effectively fixed to a low value corresponding to the initial temperature.

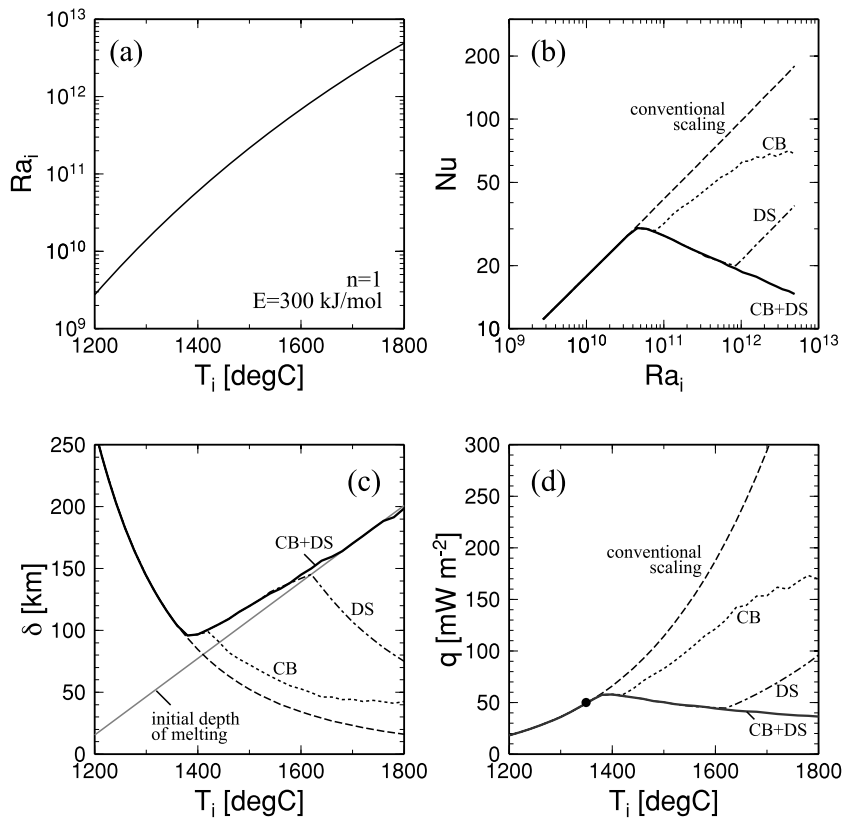


Figure 12. Scaling for stagnant-lid convection at the Earth condition. Newtonian rheology with the activation energy of 300 kJ mol^{-1} is used. Reference viscosity is chosen so that conventional scaling predicts surface heat flux of 50 mW m^{-2} at $T_i = 1350 \text{ }^\circ\text{C}$. (a) Ra_i as a function of internal temperature. (b) Nu – Ra_i relationship for conventional scaling (dashed), with the effect of compositional buoyancy (CB; dotted), with the effect of dehydration stiffening (DS; dot-dashed), and with these two effects combined (CB+DS; solid). For dehydration stiffening, $\Delta\eta = 10^2$ is assumed. For compositional buoyancy, simple mantle melting used for Fig. 11 is used. (c) Thickness of thermal boundary layer as a function of internal temperature. The initial depth of melting is also shown for comparison. (d) Predicted surface heat flux as a function of internal temperature. Solid circle denotes the reference point used to normalize viscosity.

Rehydration considered in the previous section is an important process to reduce this strong dependency on the initial condition and sustain crustal production to some extent.

In addition to hydrogen, mantle melting extracts heat-producing elements such as U and Th from the mantle, and these elements are condensed in the crust. Internal heat production in the crust insulates the mantle, and it is more appropriate to use the temperature at the crust–mantle boundary as the effective surface temperature for stagnant-lid convection (e.g. Hauck & Phillips 2002). Quite a few variables in the heat-flow scaling of eq. (56), therefore, need to be tracked self-consistently in the coupled crust–mantle evolution of a terrestrial planet.

4.5 Howard's conjecture and Buckingham π theorem

The exponent β for the Nu – Ra_i relationship (e.g. eq. 30) has commonly been set to be $1/3$ [or more generally $n/(n+2)$] in the previous studies on planetary evolution (e.g. Stevenson *et al.* 1983), and this particular value has a strong theoretical support. Because q is proportional to $Nu D$ (eq. 19) and Ra_i is proportional to $D^{(n+2)/n}$ (eqs 17 or 21), surface heat flux would become independent of the mantle depth if $\beta = n/(n+2)$. It seems natural because, for vigorous convection, surface heat flux may be controlled entirely by the dynamics of the top thermal boundary layer and may not care how deep the mantle is (e.g. Howard 1966). Note that the conventional scaling shown in Fig. 12(b) has an apparent slope of 0.37 (instead of $1/3$), but this is because θ is not constant with increasing Ra_i ;

even with a constant activation energy, θ still varies as ΔT changes (eq. 5).

The effects of mantle melting modifies this conventional scaling considerably (Fig. 12b), but it does not necessarily mean that surface heat flux becomes sensitive to the mantle depth. In fact, the new heat-flow scaling is based solely on the convective stability of the top thermal boundary layer. With mantle melting, the temperature dependency of material properties cannot be adequately parameterized by θ alone, so Nu must be a function of more than Ra_i and θ (e.g. Buckingham 1914; Barenblatt 1996). In other words, the asymptotic scaling of eq. (30) may be modified to

$$Nu \approx a\theta^{-1-\beta} Ra_i^\beta \Pi_3(T_i), \quad (62)$$

where $\Pi_3(T_i)$ is the third non-dimensional number that takes into account the effects of mantle melting at a given internal temperature. As melting is not affected by the mantle depth, Π_3 does not depend on D . The exponent β can stay as $n/(n+2)$, so surface heat flux remains independent of the mantle depth. Instead of introducing this additional non-dimensional number, one could modify β to incorporate the effects of mantle melting (e.g. Korenaga 2003) though it may give a false impression that surface heat flux depends on the mantle depth.

The conventional heat-flow scaling has been widely used when constructing a likely cooling history for terrestrial planets (e.g. Stevenson *et al.* 1983; Spohn 1991; Schubert *et al.* 1992, 1997; Nimmo & Stevenson 2000; Hauck & Phillips 2002; Breuer & Spohn

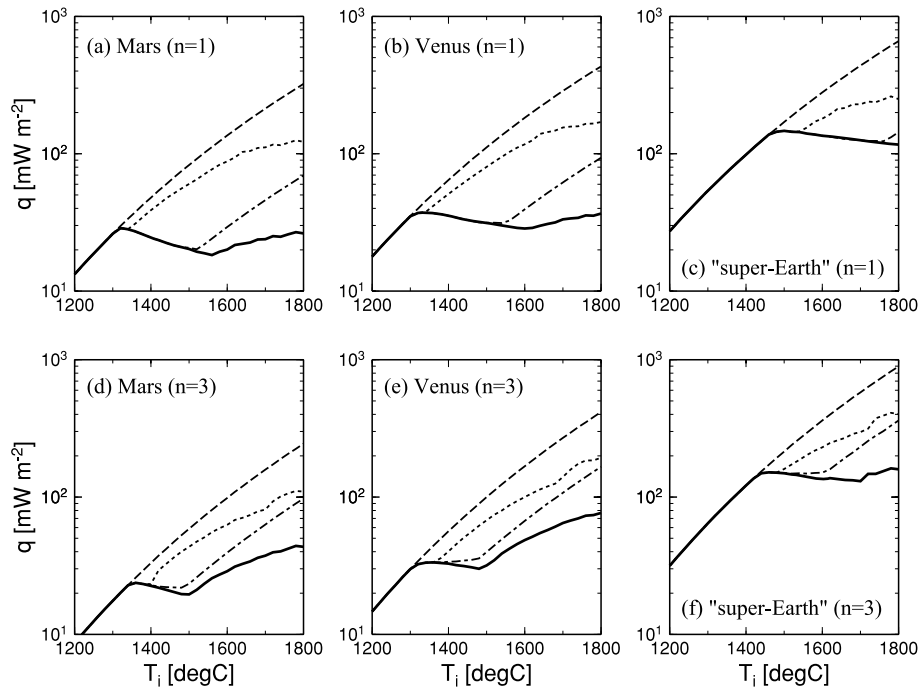


Figure 13. Preliminary heat-flow scaling laws for (a, d) Mars, (b, e) Venus, and (c, f) super-Earth. Top panel is for Newtonian rheology ($n = 1$), and bottom panel for non-Newtonian rheology ($n = 3$). As in Fig. 12, legend is conventional scaling (dashed), with compositional buoyancy alone (dotted), with dehydration stiffening alone (dot-dashed), and with both compositional buoyancy and dehydration stiffening (solid).

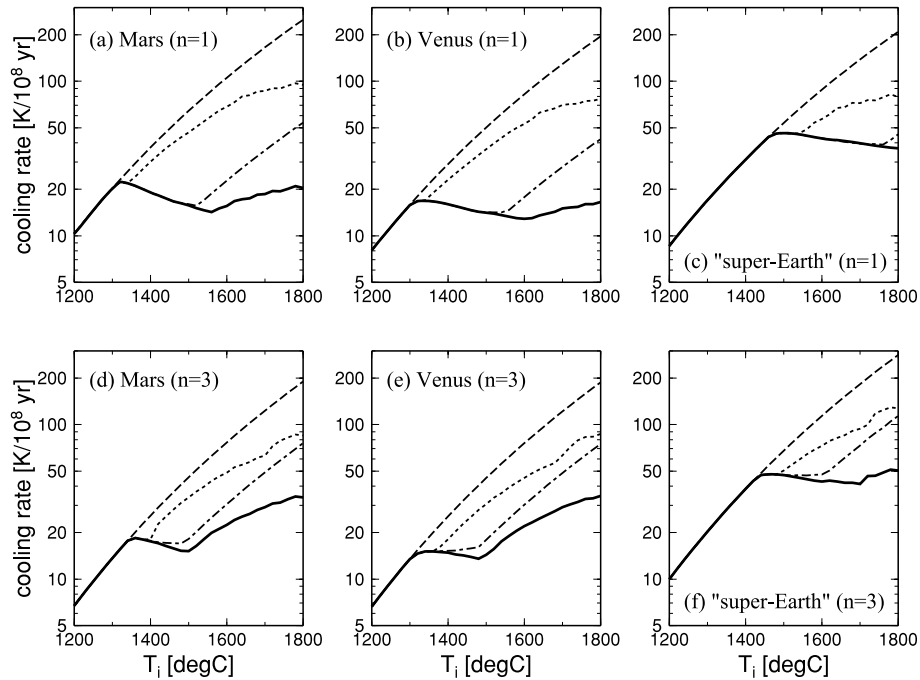


Figure 14. Nominal mantle cooling rate corresponding to surface heat flux shown in Fig. 14. Core and planetary radii are assumed as 1589 and 3389 km (Mars), 3110 and 6051 km (Venus), and 4860 and 8920 km (super-Earth), respectively, and the product of mantle density and specific heat is set to $4 \times 10^6 \text{ J m}^{-3} \text{ K}^{-1}$. Legend is the same as Fig. 13.

2003), and such cooling history has often been used as a foundation when interpreting various surface observations (e.g. Williams & Nimmo 2004; Breuer & Spohn 2006; O'Neill *et al.* 2007; Parmentier & Zuber 2007). The drastic modification of the conventional scaling, as suggested by this study, may thus lead to a major revision of our understanding of planetary evolution.

ACKNOWLEDGMENTS

The author thanks Cindy Ebinger and an anonymous reviewer for comments and suggestions. This work was sponsored by the U.S. National Science Foundation under grant EAR-0449517 and Microsoft A. Richard Newton Breakthrough Research Award.

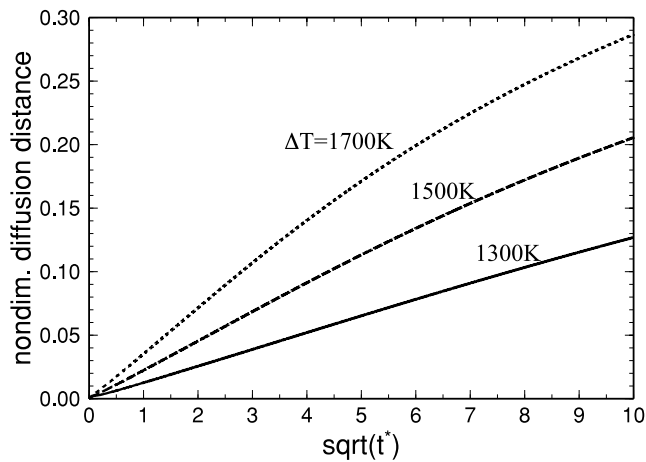


Figure 15. Hydrogen diffusion distance as a function of time. Distance is normalized by the thickness of thermal boundary layer δ , and three different values are tested for a temperature contrast across the boundary layer: 1300 K (solid), 1500 K (dashed) and 1700 K (dotted). Time is normalized by $\delta^2/D_{H,0}$, where $D_{H,0} = 6 \times 10^{-5} \text{ m}^2 \text{ s}^{-1}$.

REFERENCES

- Barenblatt, G.I., 1996. *Scaling, Self-similarity, and Intermediate Asymptotics: Dimensional Analysis and Intermediate Asymptotics*, Cambridge, New York.
- Braun, M.G., Hirth, G. & Parmentier, E.M., 2000. The effects of deep damp melting on mantle flow and melt generation beneath mid-ocean ridges, *Earth planet. Sci. Lett.*, **176**, 339–356.
- Breuer, D. & Spohn, T., 2003. Early plate tectonics versus single-plate tectonics on Mars: evidence from magnetic field history and crust evolution, *J. geophys. Res.*, **108**(E7), 5072, doi:10.1029/2002JE001999.
- Breuer, D. & Spohn, T., 2006. Viscosity of the Martian mantle and its initial temperature: constrains from crust formation history and the evolution of the magnetic field, *Planet. Space Sci.*, **54**, 153–169.
- Buckingham, E., 1914. On physically similar systems; illustrations of the use of dimensional equations, *Phys. Rev.*, **4**(4), 345–376.
- Davaille, A. & Jaupart, C., 1993. Transient high-Rayleigh-number thermal convection with large viscosity variations, *J. Fluid Mech.*, **253**, 141–166.
- Doin, M.-P., Fleitout, L. & Christensen, U., 1997. Mantle convection and stability of depleted and undepleted continental lithosphere, *J. geophys. Res.*, **102**, 2772–2787.
- Dumoulin, C., Doin, M.-P. & Fleitout, L., 1999. Heat transport in stagnant lid convection with temperature- and pressure-dependent Newtonian or non-Newtonian rheology, *J. geophys. Res.*, **104**, 12 759–12 777.
- Faul, U.H. & Jackson, I., 2007. Diffusion creep of dry, melt-free olivine, *J. geophys. Res.*, **112**, B04204, doi:10.1029/2006JB004586.
- Grasset, O. & Parmentier, E., 1998. Thermal convection in a volumetrically heated, infinite Prandtl number fluid with strongly temperature-dependent viscosity: implications for planetary thermal evolution, *J. geophys. Res.*, **103**, 18 171–18 181.
- Hauk, S.A. & Phillips, R.J., 2002. Thermal and crustal evolution of Mars, *J. geophys. Res.*, **107**(E7), 5052, doi:10.1029/2001JE001801.
- Hirth, G. & Kohlstedt, D.L., 1996. Water in the oceanic mantle: implications for rheology, melt extraction, and the evolution of the lithosphere, *Earth planet. Sci. Lett.*, **144**, 93–108.
- Howard, L.N., 1966. Convection at high Rayleigh number, in *Proceedings of the Eleventh International Congress of Applied Mechanics*, pp. 1109–1115, ed. Gortler, H., Springer-Verlag, New York.
- Johnson, M.C., Rutherford, M.J. & Hess, P.C., 1991. Chassigny petrogenesis: melt compositions, intensive parameters, and water contents of Martian (?) magmas, *Geochim. Cosmochim. Acta*, **55**, 349–366.
- Karato, S. & Wu, P., 1993. Rheology of the upper mantle: a synthesis, *Science*, **260**, 771–778.
- Koga, K., Hauri, E., Hirschmann, M. & Bell, D., 2003. Hydrogen concentration analysis using SIMS and FTIR: comparison and calibration for nominally anhydrous minerals, *Geochim. Geophys. Geosys.*, **4**, 1019, doi:10.1029/2002GC000378.
- Kohlstedt, D.L., 1992. Structure, rheology and permeability of partially molten rocks at low melt fractions, in *Mantle Flow and Melt Generation at Mid-Ocean Ridges*, Vol. **71**, pp. 103–121, eds Phipps Morgan, J., Blackman, D.K. & Sinton, J.M., *Geophys. Monogr. Ser.*, AGU, Washington, DC.
- Korenaga, J., 2003. Energetics of mantle convection and the fate of fossil heat, *Geophys. Res. Lett.*, **30**(8), 1437, doi:10.1029/2003GL016982.
- Korenaga, J., 2006. Archean geodynamics and the thermal evolution of Earth, in *Archean Geodynamics and Environments*, pp. 7–32, eds Benn, K., Mareschal, J.-C. & Condie, K., American Geophysical Union, Washington, DC.
- Korenaga, J. & Jordan, T.H., 2003. Physics of multiscale convection in Earth's mantle: onset of sublithospheric convection, *J. geophys. Res.*, **108**(B7), 2333, doi:10.1029/2002JB001760.
- Korenaga, J. & Karato, S., 2008. A new analysis of experimental data on olivine rheology, *J. geophys. Res.*, **113**, B02403, doi:10.1029/2007JB005100.
- Lunine, J.I., Chambers, J., Morbidelli, A. & Leshin, L.A., 2003. The origin of water on Mars, *Icarus*, **165**, 1–8.
- Mackwell, S.J. & Kohlstedt, D.L., 1990. Diffusion of hydrogen in olivine: implications for water in the mantle, *J. geophys. Res.*, **95**, 5079–5088.
- Mei, S. & Kohlstedt, D.L., 2000a. Influence of water on plastic deformation of olivine aggregates. 1: diffusion creep regime, *J. geophys. Res.*, **105**, 21 457–21 469.
- Mei, S. & Kohlstedt, D.L., 2000b. Influence of water on plastic deformation of olivine aggregates. 2: dislocation creep regime, *J. geophys. Res.*, **105**, 21 471–21 481.
- Morris, S. & Canright, D., 1984. A boundary-layer analysis of benard convection in a fluid of strongly temperature-dependent viscosity, *Phys. Earth planet. Int.*, **36**, 355–373.
- Mysen, B.O., Virgo, D., Popp, R.K. & Bertka, C.M., 1998. The role of H₂O in Martian magmatic systems, *Am. Mineral.*, **83**, 942–946.
- Nimmo, F. & Stevenson, D.J., 2000. Influence of early plate tectonics on the thermal evolution and magnetic field of Mars, *J. geophys. Res.*, **105**(E5), 11 969–11 979.
- Ogawa, M., Schubert, G. & Zebib, A., 1991. Numerical simulations of three-dimensional thermal convection in a fluid with strongly temperature-dependent viscosity, *J. Fluid Mech.*, **233**, 299–328.
- O'Neill, C., Lenardic, A., Jellinek, A.M. & Kiefer, W.S., 2007. Melt propagation and volcanism in mantle convection simulation, with applications for Martian volcanic and atmospheric evolution, *J. geophys. Res.*, **112**, E07003, doi:10.1029/2006JE002799.
- Parmentier, E.M. & Hess, P.C., 1992. Chemical differentiation of a convecting planetary interior: consequences for a one plate planet such as Venus, *Geophys. Res. Lett.*, **19**, 2015–2018.
- Parmentier, E.M. & Zuber, M.T., 2007. Early evolution of Mars with mantle compositional stratification or hydrothermal crustal cooling, *J. geophys. Res.*, **112**, E02007, doi:10.1029/2005JE002626.
- Reese, C.C., Solomatov, V.S. & Moresi, L.-N., 1999. Non-newtonian stagnant lid convection and magmatic resurfacing on Venus, *Icarus*, **139**, 67–80.
- Schubert, G., Solomon, S.C., Turcotte, D.L., Drake, M.J. & Sleep, N.H., 1992. Origin and thermal evolution of Mars, pp. 147–183, eds Kieffer, H.H., Jakosky, B.M., Snyder, C.W. & Matthews, M.S., University of Arizona Press, Tucson, AZ.
- Schubert, G., Solomatov, V.S., Tackley, P.J. & Turcotte, D.L., 1997. Mantle convection and the thermal evolution of Venus, in *Venus II*, pp. 1245–1287, University of Arizona Press, Tucson, AZ.
- Schubert, G., Turcotte, D.L. & Olson, P., 2001. *Mantle Convection in the Earth and Planets*, Cambridge Univ. Press, New York.
- Solomatov, V.S., 1995. Scaling of temperature- and stress-dependent viscosity convection, *Phys. Fluids*, **7**, 266–274.

- Solomatov, V.S. & Moresi, L.-N., 1996. Stagnant lid convection on Venus, *J. geophys. Res.*, **101**(E2), 4737–4753.
- Solomatov, V.S. & Moresi, L.-N., 2000. Scaling of time-dependent stagnant lid convection: application to small-scale convection on earth and other terrestrial planets, *J. geophys. Res.*, **105**, 21 795–21 817.
- Spohn, T., 1991. Mantle differentiation and thermal evolution of Mars, Mercury, and Venus, *Icarus*, **90**, 222–236.
- Stevenson, D.J., Spohn, T. & Schubert, G., 1983. Magnetism and thermal evolution of the terrestrial planets, *Icarus*, **54**, 466–489.
- Tackley, P.J., 2000. Self-consistent generation of tectonic plates in time-dependent, three-dimensional mantle convection simulations. 2: strain weakening and asthenosphere, *Geochem. Geophys. Geosys.*, **1**, doi:10.1029/2000GC000043.
- Takahashi, E. & Kushiro, I., 1983. Melting of a dry peridotite at high pressures and basalt magma genesis, *Am. Mineral.*, **68**, 859–879.
- Valencia, D., Sasselov, D.D. & O’Connell, R.J., 2007. Radius and structure models of the first super-Earth planet, *Astrophys. J.*, **656**, 545–551.
- van Thienen, P., 2007. Convective vigour and heat flow in chemically differentiated systems, *Geophys. J. Int.*, **169**, 747–766.
- Wänke, H. & Dreibus, G., 1994. Chemistry and accretion of Mars, *Philos. Trans. R. Soc. Lond. A*, **349**, 2134–2137.
- Williams, J.-P. & Nimmo, F., 2004. Thermal evolution of the Martian core: implications for an early dynamo, *Geology*, **32**, 97–100.